Electronic Supplementary Information

for

Environmental Science: Nano

Arsenic species delay structural ordering during green rust sulfate crystallization from ferrihydrite†

Jeffrey Paulo H. Perez,*[,a,b] Dominique J. Tobler,[c,d] Helen M. Freeman,[e] Andy P. Brown,[e] Nicole S. Hondow,[e] Case M. van Genuchten,[f] Liane G. Benning[a,b]

[a] *Sec. 3.5 Interface Geochemistry, GFZ German Research Center for Geosciences, Telegrafenberg, 14473 Potsdam, Germany. E-mail: jpperez@gfz-potsdam.de*

[b] *Department of Earth Sciences, Freie Universität Berlin, 12249 Berlin, Germany*

[c] *Nano-Science Center, Department of Chemistry, University of Copenhagen, 2100 Copenhagen, Denmark*

[d] *Department of Plant and Environmental Sciences, University of Copenhagen, 1871 Frederiksberg C, Denmark*

[e] *Leeds Electron Microscopy and Spectroscopy Centre (LEMAS), School of Chemical and Process Engineering, University of Leeds, Leeds LS2 9JT, United Kingdom*

[f] *Geological Survey of Denmark and Greenland (GEUS), 1350 Copenhagen, Denmark*

This supporting information contains: 9 pages, 7 figures, 2 tables.

Text S1. Preliminary experiments on the As-free Fe^{2+}-induced transformation of ferrihydrite (FHY) to green rust sulfate (GR_{SO4})

The mineralogical composition of the solids during the Fe^{2+}-induced transformation of ferrihydrite (FHY) at circum-neutral pH is largely dependent on the ratio between dissolved [Fe^{2+}] and the $[Fe(III)]_{FHY}$ in the system (Boland et al., 2014; Hansel et al., 2005). To properly quantify the formation kinetics, we need to ensure that the $Fe^{2+}_{(aq)}/Fe(III)_{FHY}$ ratio used in the transformation experiments results in green rust sulfate (GR_{SO4}) as the sole crystalline Fe phase. We therefore performed preliminary As-free transformation experiments with varying $Fe^{2+}_{(aq)}/Fe(III)_{FHY}$ ratios at pH 8 inside the anaerobic chamber. In brief, varying amounts of an 0.5 M $Fe^{II}SO_4$ stock solution were added to the FHY suspensions ($[Fe(III)]_{FHY}$ ≈ 4.2 mM) in a 0.1 M NaCl background electrolyte, achieving the $Fe^{2+}_{(aq)}/Fe(III)_{FHY}$ ratios (R) of 0.25, 0.5, 1, 2 and 3. The pH of the suspension was maintained at ~8 using a titrator (Metrohm 785 DMP) with 1 M NaOH under stirring at 350 rpm. After one hour, 10-mL aliquots from the reaction vessels were vacuum filtered through a 0.22-µm polycarbonate membrane filter. The wet sample pastes were loaded onto an X-ray transparent dome sample holder to prevent GR_{SO4} oxidation, and then analyzed by powder X-ray diffraction (XRD) to determine the mineralogical composition of the solids. The XRD patterns of the transformation products are shown in Figure S1.

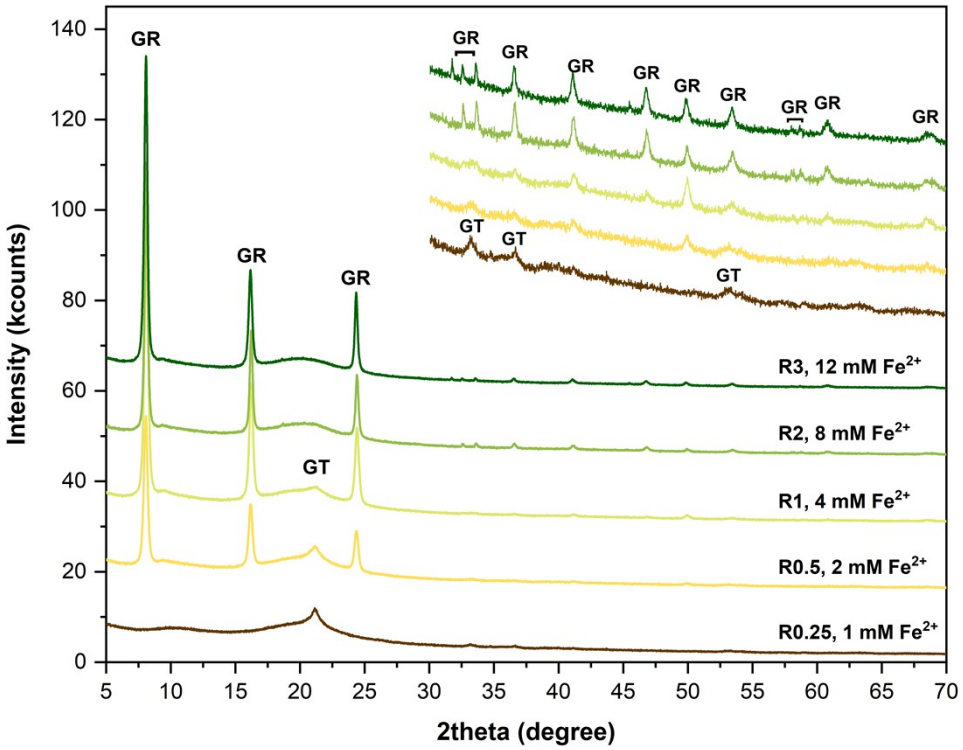

Figure S1. XRD patterns showing the mineralogical composition of the solids, 1 h after the addition of varying $[Fe^{2+}]_{(aq)}$ (ca. 1-12 mM) to ferrihydrite ($[Fe(III)_{FHY}]$ = 4 mM) in the As-free system at pH 8. The $Fe^{2+}_{(aq)}/Fe(III)_{FHY}$ ratios (R) tested ranged between 0.25 to 3. The amorphous hump at ~11 and ~20° comes from the X-ray transparent dome. Note: GR – GR sulfate (GR_{SO4}) and GT – goethite.

Text S2. Elemental concentration analysis by ICP-OES

Sample dilutions were done using 0.3 M HNO_3 (Merck Suprapure grade) containing 1 mg g^{-1} Cs as an ionization buffer to achieve matrix matching with calibration standards prepared from a mixture of single ICP element standards (Merck certipur, traceable to NIST reference materials). Scandium (1 µg g^{-1}) was added as an internal standard. Dilution factors were adapted to ensure that analyte solutions were within the concentration range of the matrix-matched calibration standards (linearity criteria $R^2 > 0.9990$) and with final HNO_3 and Cs concentrations of 0.3 M and 1 mg g^{-1}, respectively.

Instrumental stability and drift were monitored using Ar, Cs and Sc at emission wavelengths of 420.067, 459.311 and 335.372 nm for each sample analysis, respectively, as well as regular measurements of a quality control (QC) solution, similar to sample compositions. Instrumental statistical limits of detection (LoD = 3SD above background) or limits of quantification (LoQ = 10SD above background) were determined in each analytical session based on nine repeat analysis of 0.3 M HNO_3 (+ 1 mg g^{-1} Cs) used for sample dilution.

The determined LoD and LoQ for As were 0.015 and 0.044 µg g^{-1}, respectively. Detection limits translate to maximum detectable removal efficiency of >99.8%. Analytical uncertainties at a 95% confidence level for concentrations quantified (above LoQ) during this study are ~5% relative, verified by repeat analyses of a QC solution, which was similar to the sample compositions (Table S1).

Table S1. ICP-OES data for quality control solutions (QC) that were prepared from single element standard solutions (Merck, CertiPur) to achieve chemical compositions similar to the experimental sample solutions. The mean results of *n* replicate analyses are given together with the standard deviation (SD) and relative standard deviation (RSD) (SD represents 68% of the population, 2SD represents 95% of the population). The measured deviation from the reference value is a quantitative estimation of accuracy.

	As (mg L^{-1})	Fe (mg L^{-1})	S (mg L^{-1})
Wavelength	193.696	261.382	181.972
Instrumental limits			
Limit of detection (LoD)	0.015	0.171	0.233
Limit of quantification (LoQ)	0.044	0.373	0.521
Quality control			
QC verify (*n* = 9)	0.574	6.301	6.298
SD	0.010	0.061	0.020
RSD	1.67%	1.94%	0.32%
2RSD	3.34%	1.94%	0.65%
Reference value	0.579	6.284	6.222
Uncertainty	0.003	0.063	0.008
Measured deviation from reference value	0.86%	0.26%	1.22%

Text S3. As K-edge X-ray absorption spectroscopy

Dry powders of each solid samples were transported to the XAS beamline inside air-tight headspace crimp vials stored inside an anaerobic jar to prevent oxidation during sample transport. Prior to data collection, pellets were prepared inside a station glovebox (MBRAUN, Ar atmosphere) by mixing the dry powder samples with cellulose using an agate mortar and pestle. Mixture calculations were done using XAFSmass software (Klementiev and Chernikov, 2016). The pellets were sealed inside sample holders made of 2 layers of single-sided 70-µm thick Kapton® polyimide tape. The Kapton-sealed samples were fixed onto a beamline custom-specific sample holder and transferred to the station using the anaerobic jar.

Arsenic K-edge XAS data were collected at BM23 of the European Synchrotron Radiation Facility (ESRF, Grenoble, France; Mathon et al. (2015)). Spectra were recorded at liquid nitrogen temperatures (77 K) both in transmission and fluorescence mode out to a reciprocal space value of 14 $Å^{-1}$. For this, a cryostat was used with helium convection. Fluorescence data were collected using an Si vortex detector. The vertical dimension of the X-ray beam during data collection was 1 mm and the horizontal dimension was 2 mm. To prevent second-order harmonics, rejection mirrors were used. A Si(111) crystal pair with a fixed beam exit was used as a monochromator and the maximum in the first derivative of an Au foil was used to calibrate the beam at 11919 eV (Au L_3 edge). The XANES region was measured with 0.35 eV steps. About 4 to 6 scans were collected for each sample depending on data quality. During data collection, changes in line shape and peak position indicative of beam-induced redox reactions were examined and no beam damage was observed. Spectra were aligned, averaged, and background-subtracted using the SIXpack software (Webb, 2005).

Shell-by-shell fits were performed from 1 to 4 Å in R+ΔR-space using SIXPack software (Webb, 2005), based on algorithms derived from IFEFFIT (Newville, 2001). The fits typically included the interatomic distance (R), the coordination number (CN), the mean squared atomic displacement parameter (σ^2), and the change in threshold energy (ΔE_0) for one sample. Phase and amplitude functions for single and multiple scattering paths were calculated using FEFF6 (Rehr et al., 1992) and included As-O, As-O-O and As-Fe paths derived from the structure of scorodite (Kitahama et al., 1975). In preliminary fits, the CN and σ^2 were found to be highly correlated, which produced high fit-derived standard errors in these fitting parameters. Therefore, following previous work (Mikutta et al., 2010; van Genuchten et al., 2012), we constrained σ^2 to 0.009 in the second shell fits (As-Fe path) to reduce the high correlations. Consistent with previous work (Mikutta et al., 2010; Paktunc et al., 2008), the passive electron reduction parameter, S_0^2, in each fit was set to 1.0. The goodness-of-fit was assessed based on the R-factor, which is defined as the mean square difference between the fit and the data on a point-by-point basis: $R = \sum_i (data_i - fit_i)^2 / \sum_i (data_i)^2$. An R-factor <0.05 is considered to reflect a reasonable fit (Kelly et al., 2008).

S4. Supplementary Figures

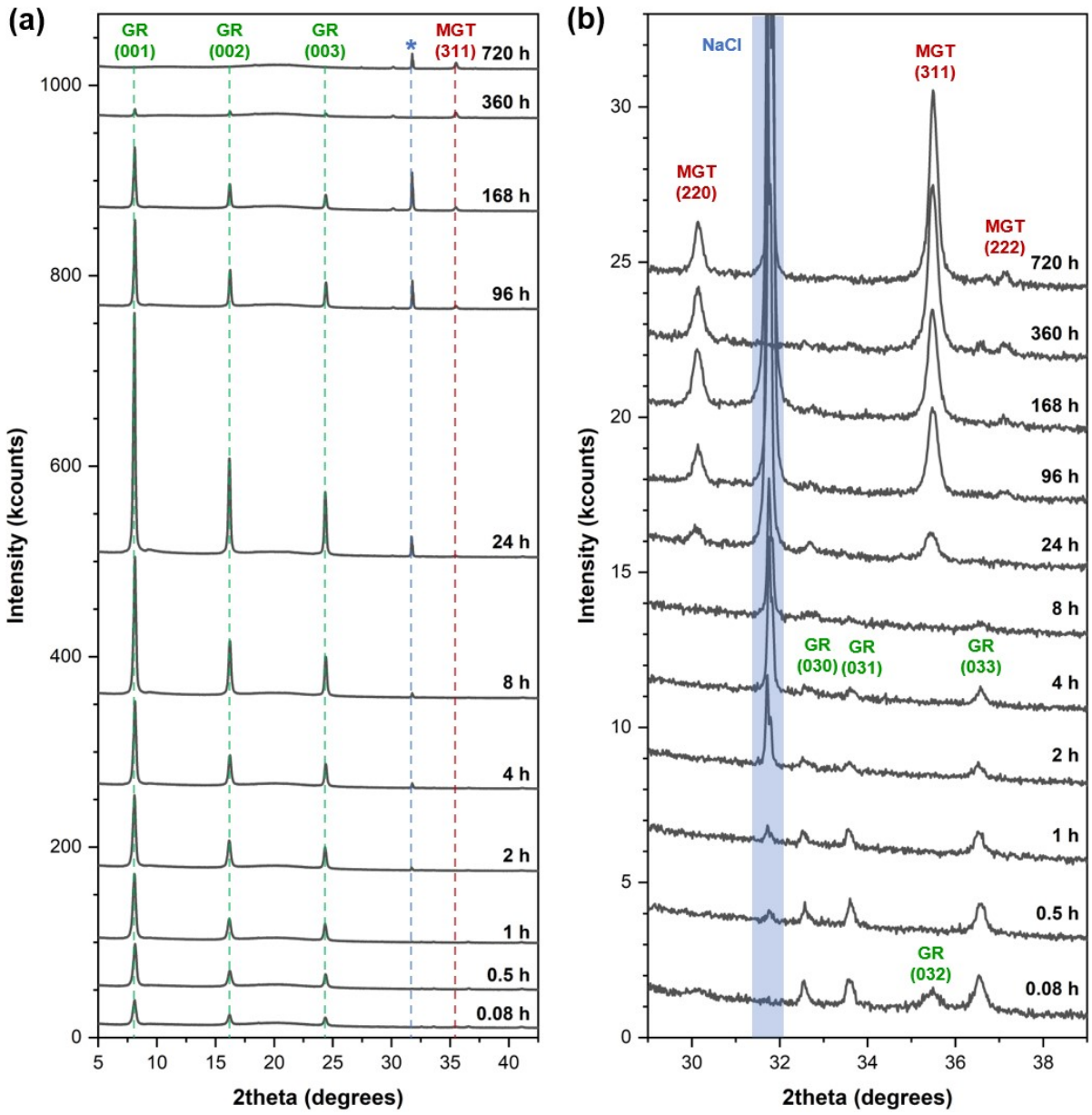

Figure S2. (a) XRD patterns showing the change in mineralogical composition of the solid samples during the transformation of ferrihydrite in the As-free system at an $Fe^{2+}_{(aq)}/Fe(III)_{FHY}$ ratio of 3 and pH 8. Note: GR – GR sulfate (GR_{SO4}); MGT – magnetite; and the * symbol marks peaks corresponding to halite (NaCl). The 2theta ranges in (a) are clipped from 5 to 42.5° for clarity. The increased peak intensities of the basal (00*l*) reflections of GR_{SO4} arise from the preferential orientation of the GR_{SO4} plates along the [001] zone axis during XRD sample preparation. (b) Zoomed XRD patterns from (a), clipped over the 2theta range of 28 to 39°, showing the appearance of MGT peaks within 24 h of reaction. The blue semi-transparent bar corresponds to the NaCl peak. Note that NaCl is present because the solids were not washed during filtration to avoid any potential, further transformation of GR (Thomas et al., 2018).

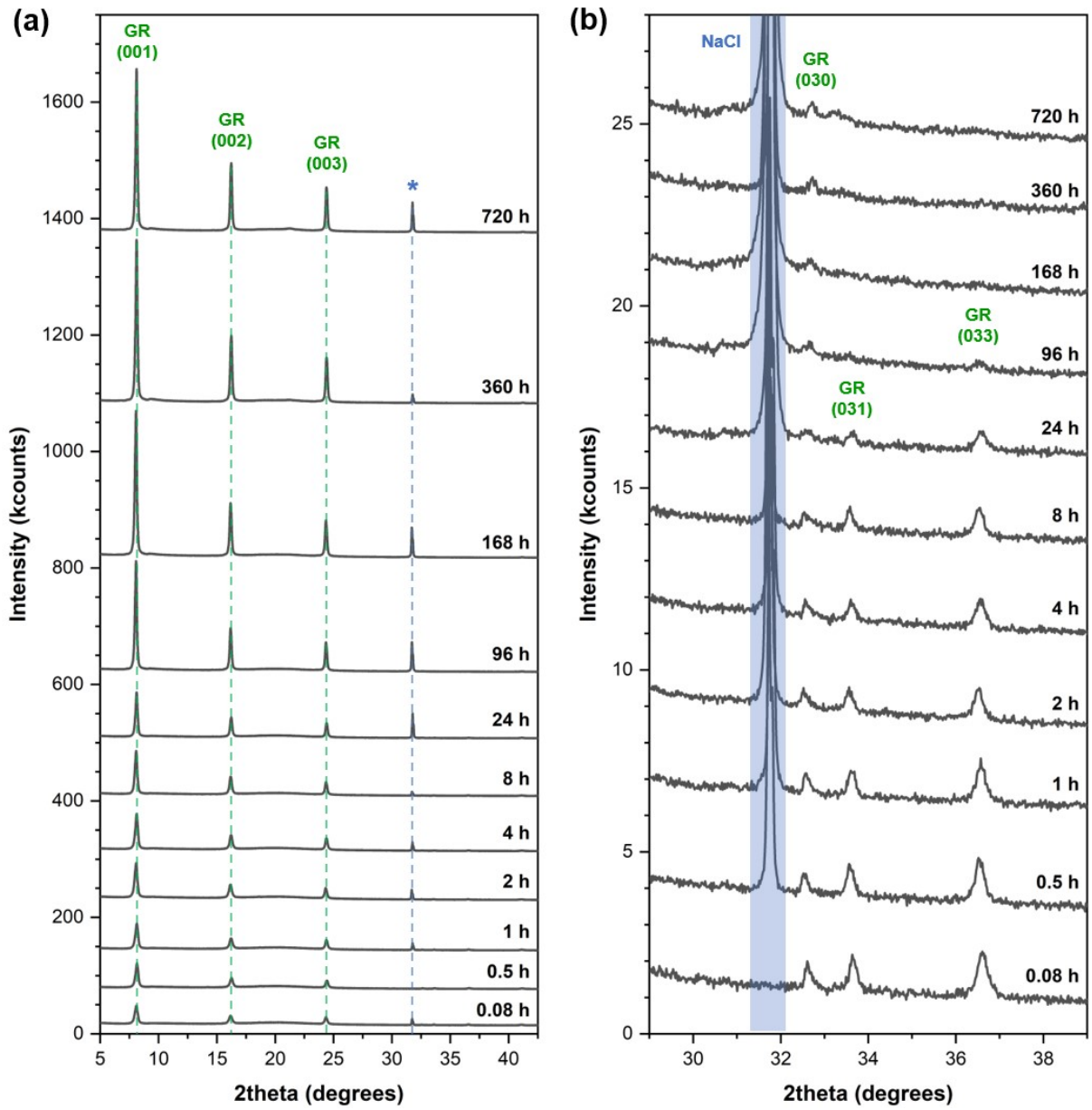

Figure S3. (a) XRD patterns showing the change in mineralogical composition of the solid samples during the transformation of As(III)-bearing ferrihydrite at an $Fe^{2+}_{(aq)}/Fe(III)_{FHY}$ ratio of 3 and pH 8. (b) Zoomed XRD patterns from (a) shows that MGT was not detected over the 720-h transformation of As(III)-bearing ferrihydrite.

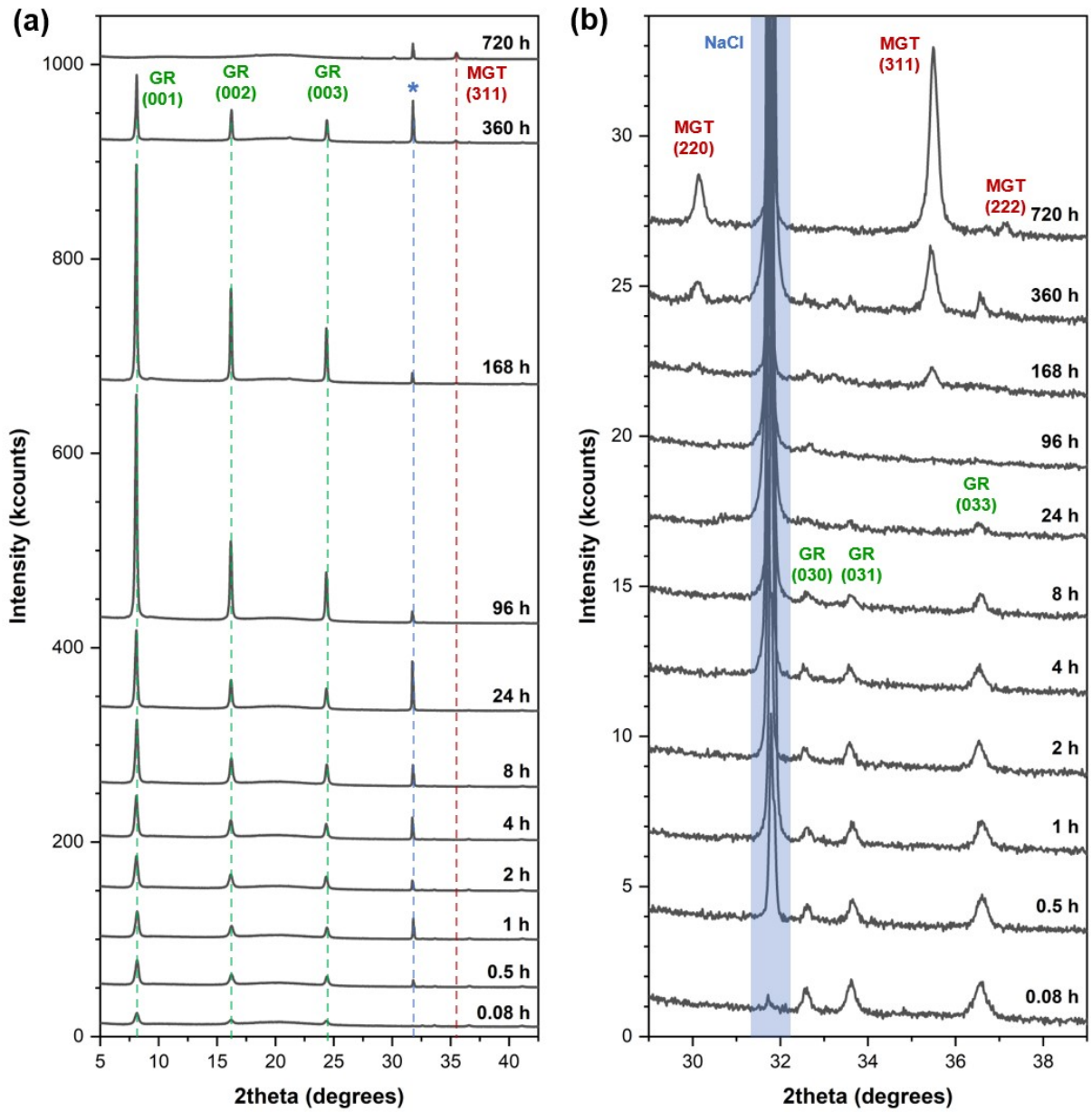

Figure S4. (a) XRD patterns showing the change in mineralogical composition of the solid samples during the transformation of As(V)-bearing ferrihydrite at an $Fe^{2+}_{(aq)}/Fe(III)_{FHY}$ ratio of 3 and pH 8. (b) Zoomed XRD patterns from (a) showing the appearance of MGT peaks within 168 h (7 d) of reaction.

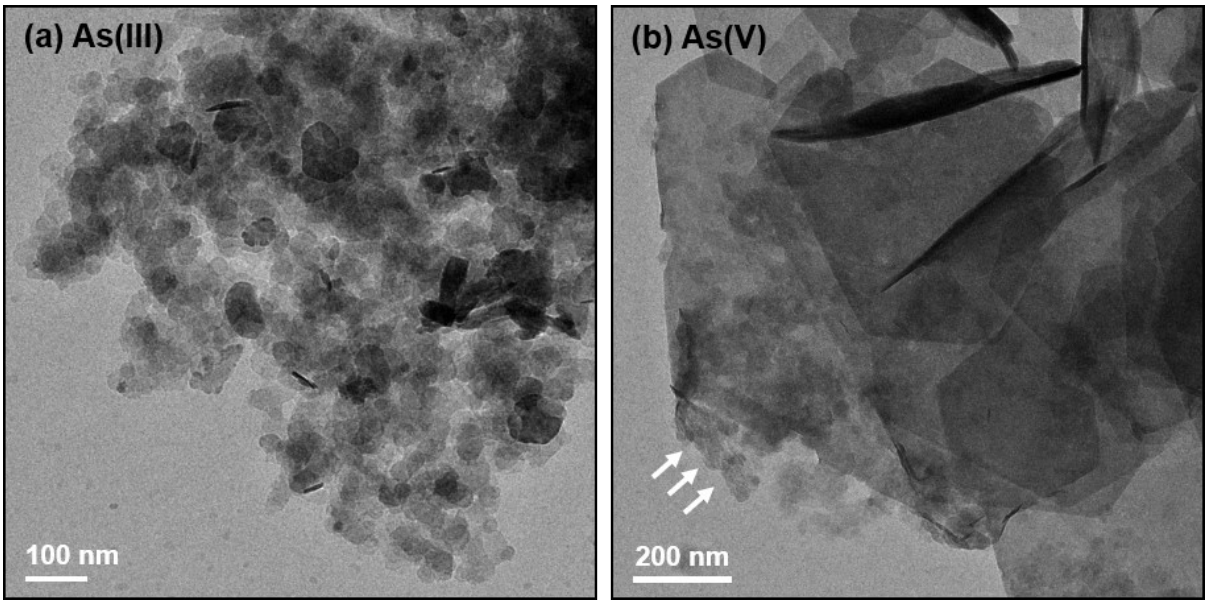

Figure S5. TEM images of the cryo-quenched As(III)- and As(V)-bearing precipitates after 7 d (168 h) of reaction: (a) Aggregates of the nano-sized As(III)-bearing GR_{SO4}. (b) As(V)-bearing GR_{SO4} hexagonal plates with associated nano-sized platelets (white arrows).

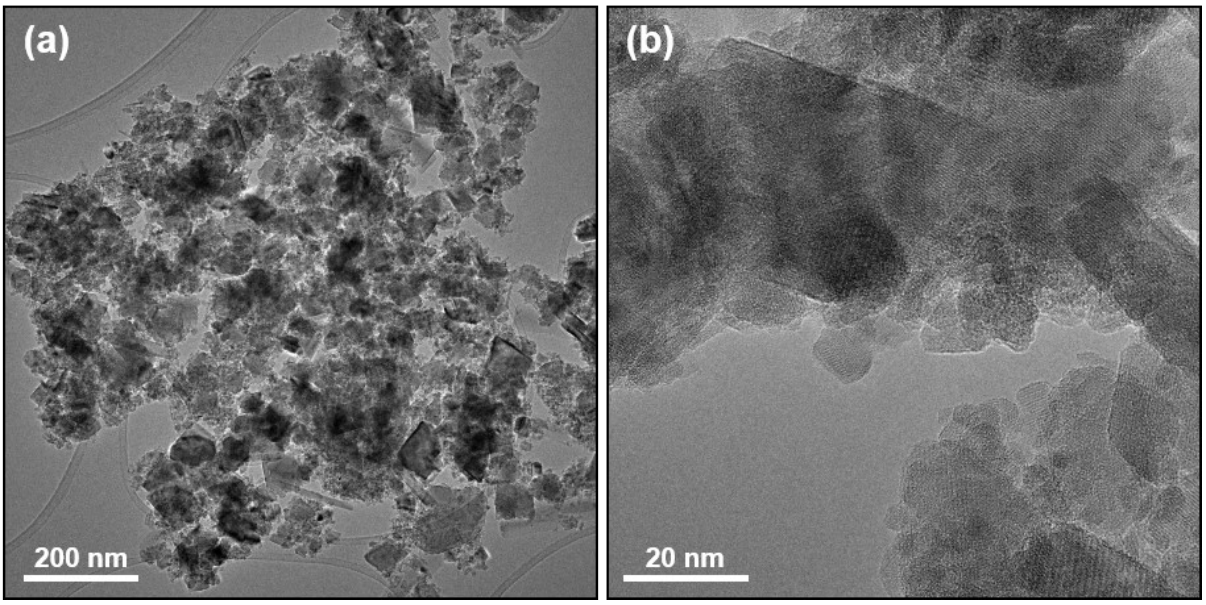

Figure S6. TEM images of the As(V)-bearing MGT: (a) overview and (b) close-up TEM images showing the two different morphologies of the MGT nanoparticles.

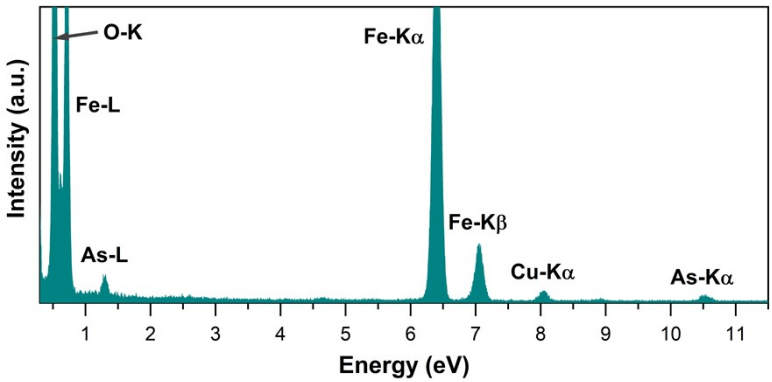

Figure S7. Energy dispersive X-ray (EDX) spectrum of the As(V)-reacted MGT solids after 720 h.

References

Boland, D. D., Collins, R. N., Miller, C. J., Glover, C. J. and Waite, T. D. (2014) Effect of solution and solid-phase conditions on the Fe(II)-accelerated transformation of ferrihydrite to lepidocrocite and goethite. *Environ. Sci. Technol.* **48**, 5477-5485.

Hansel, C. M., Benner, S. G. and Fendorf, S. (2005) Competing Fe (II)-induced mineralization pathways of ferrihydrite. *Environ. Sci. Technol.* **39**, 7147-7153.

Kelly, S. D., Hesterberg, D. and Ravel, B. (2008) Analysis of soils and minerals using X-ray absorption spectroscopy, in: Ulery, A.L., Drees, L.R. (Eds.), Methods of Soil Analysis Part 5—Mineralogical methods. Soil Science Society of America, Madison, WI.

Kitahama, K., Kiriyama, R. and Baba, Y. (1975) Refinement of the crystal structure of scorodite. *Acta Crystallographica Section B: Structural Crystallography and Crystal Chemistry* **31**, 322-324.

Klementiev, K. and Chernikov, R. (2016) XAFSmass: A program for calculating the optimal mass of XAFS samples. *J. Phys. Conf. Ser.* **712**, 012008.

Mathon, O., Beteva, A., Borrel, J., Bugnazet, D., Gatla, S., Hino, R., Kantor, I., Mairs, T., Munoz, M., Pasternak, S., Perrin, F. and Pascarelli, S. (2015) The time-resolved and extreme conditions XAS (TEXAS) facility at the European Synchrotron Radiation Facility: The general-purpose EXAFS bending-magnet beamline BM23. *J. Synchr. Radiat.* **22**, 1548-1554.

Mikutta, C., Frommer, J., Voegelin, A., Kaegi, R. and Kretzschmar, R. (2010) Effect of citrate on the local Fe coordination in ferrihydrite, arsenate binding, and ternary arsenate complex formation. *Geochim. Cosmochim. Acta* **74**, 5574-5592.

Newville, M. (2001) IFEFFIT: interactive XAFS analysis and FEFF fitting. *J Synchrotron Radiat* **8**, 322-324.

Paktunc, D., Dutrizac, J. and Gertsman, V. (2008) Synthesis and phase transformations involving scorodite, ferric arsenate and arsenical ferrihydrite: Implications for arsenic mobility. *Geochim. Cosmochim. Acta* **72**, 2649-2672.

Rehr, J. J., Albers, R. C. and Zabinsky, S. I. (1992) High-order multiple-scattering calculations of x-ray-absorption fine structure. *Phys. Rev. Lett.* **69**, 3397-3400.

Thomas, A. N., Eiche, E., Göttlicher, J., Steininger, R., Benning, L. G., Freeman, H. M., Dideriksen, K. and Neumann, T. (2018) Products of hexavalent chromium reduction by green rust sodium sulfate and associated reaction mechanisms. *Soil Syst.* **2**, 58.

van Genuchten, C. M., Addy, S. E., Pena, J. and Gadgil, A. J. (2012) Removing arsenic from synthetic groundwater with iron electrocoagulation: an Fe and As K-edge EXAFS study. *Environ. Sci. Technol.* **46**, 986-994.

Webb, S. M. (2005) SIXpack: a graphical user interface for XAS analysis using IFEFFIT. *Phys. Scr.* **T115**, 1011-1014.